Plasmonic Force Propulsion for Small Spacecraft

Joshua L. Rovey,[*] Xiaodong Yang,[†] Paul D. Friz,[‡] Changyu Hu,[§] and Matthew S. Glascock[**]
Missouri University of Science and Technology, Rolla, Missouri, 65409

Plasmonic force propulsion uses solar light focused on deep-subwavelength nanostructures to excite strong optical forces that accelerate and expel nanoparticle propellant. The concept was assessed within the context of precision pointing and position control for nano/pico-satellites. Plasmonic force fields were numerically simulated, propulsion performance predicted and then used to evaluate spacecraft position control resolution and pointing precision. Results for a conceptual design of a plasmonic thruster that has 35 layers, 86 array columns, multi-stage length of 5 mm, a 5-cm-diameter light focusing lens, and uses 100 nm polystyrene nanoparticles expelled at a rate of 1×10^6 per sec would have a thrust of 250 nN, specific impulse of 10 sec, and minimum impulse bit of 50 pN-s. The thruster mass and volume are estimated at 100 g and 50 cm^3, respectively. Results predict plasmonic force propulsion can enhance the state-of-the-art in small spacecraft position and attitude control by 1-2 orders of magnitude. This has the potential to enable advanced missions that require ultra-fine pointing precision to less than 0.1 milliarcsecond.

Nomenclature

A	=	area [m^2]
B	=	magnetic field [T]
E	=	electric field [V/m]
F	=	force [N]
I	=	intensity [W/m^2]
I_{sp}	=	specific impulse [sec]
J	=	current density [A/m^2]
L	=	acceleration length [m]
M_e	=	mass expended [kg]
N	=	number of array elements
P	=	power [W]
T	=	thrust [N]
T_{ij}	=	Maxwell stress tensor
V	=	volume [m^3] or velocity [m/s]
a	=	acceleration [m/s^2]
f	=	force per unit volume [N/m^3] or expulsion rate [sec^{-1}]
g_o	=	gravitational constant [9.81 m/s^2]
m	=	mass [kg]
t	=	time [sec]
v	=	velocity [m/s]

---

[*] Associate Professor of Aerospace Engineering, Mechanical and Aerospace Engineering, 292D Toomey Hall, 400 W. 13th Street, Senior Member AIAA.

[†] Assistant Professor of Mechanical Engineering, Mechanical and Aerospace Engineering, Toomey Hall, 400 W. 13th Street.

[‡] Graduate Research Assistant, Aerospace Plasma Laboratory, Mechanical and Aerospace Engineering, 160 Toomey Hall, 400 W. 13th Street, Student Member AIAA.

[§] Graduate Research Assistant, NanoOptics Laboratory, Mechanical and Aerospace Engineering, Toomey Hall, 400 W. 13th Street.

[**] Undergraduate Research Assistant, Aerospace Plasma Laboratory, Mechanical and Aerospace Engineering, 160 Toomey Hall, 400 W. 13th Street, Student Member AIAA.

x	=	position [m]
ρ	=	charge density [C/m^3]
ε_o	=	permittivity of free space
μ_o	=	permeability of free space
δ_{ij}	=	Kronecker delta function

I. Introduction

INTEREST in small spacecraft continues to increase in government, commercial, and academic sectors. According to a recent SpaceWorks report on the nano/microsatellite market, the number of small satellites being developed and launched will continue to increase over the next 7 to 10 years from 35 launched in 2012 to an anticipated 188 launched in 2020 [1]. Defense and intelligence interest in nanosatellites is expected to increase from only 8% of launches today to almost 40% by 2015. The recent Air Force Global Horizons report specifically lists fractionated constellations of small spacecraft as a game-changing technology of focus over the next 15-20 years [2]. NASA continues to develop science and exploration mission scenarios for small spacecraft [3], such as asteroid mapping, Earth observing, deployable x-ray telescopes, exoplanet observatories, and constellations of spacecraft for Earth and deep space observations.

In spite of the intense and exploding interest in small spacecraft, their full potential remains untapped because they lack maneuverability. The major challenge remains propulsion. Micci and Ketsdever [4] compiled micropropulsion state-of-the-art in 2000. And many of those micropropulsion systems have been or are being investigated for small spacecraft (e.g., microresistojets, microcavity discharge thrusters, mini ion/Hall, pulsed plasma thrusters, and electrospray MEMS). New concepts have also been investigated (e.g., nanoparticle field extraction, laser ablation, free molecule resistojet). While significant advances have been made, small spacecraft still lack propulsion for the same reasons outlined by Micci and Ketsdever: mass, power, and volume constraints. The need remains for a propulsion system that can fit on ever-shrinking small nano/pico spacecraft platforms.

The following sections describe and analyze a new concept for providing maneuverability for small spacecraft. First the concept of plasmonic space propulsion is described. Then the concept is analyzed by predicting the strength of the plasmonic force field, propulsion performance, and small spacecraft maneuverability with a conceptual thruster design. Specifically the ability of a plasmonic thruster system to provide precision alignment and proximity control for a small spacecraft is determined and compared with other state-of-the-art propulsion and torquer systems. Finally, conclusions are drawn based on the analysis and comparison.

II. Plasmonic Force Propulsion Concept

The plasmonic force propulsion concept is built upon the growing field of plasmonics, which exploits the unique optical properties of metallic nanostructures to route and manipulate light at nanometer length scales. Plasmonic antennas and lenses can focus optical radiation into intense, engineered, localized field distributions or enable coupling to deep-subwavelength guided modes. Enhanced plasmonic forces enable manipulation and acceleration of nanoparticles, in what is commonly referred to as "optical tweezers."[5-7] The concept is illustrated in Figure 1. Sun light is directly focused onto deep-subwavelength metallic nanostructures through a lens. The resonant interaction and coupling of the light with the nanostructure excites surface plasmon polaritons that generate a strong gradient optical force field. Nanoparticles (e.g., glass beads or metallic particles) are accelerated by the gradient force field and are expelled from the device at high speeds. Because the optical force field is coupled to the nanostructure through the strong light-matter interaction with surface plasmon polaritons, thrust is generated through momentum exchange with the expelled particles.

Careful examination of Figure 1 reveals a major benefit of the concept: no electric or spacecraft power required. Solar energy is directly converted into propulsive thrust (jet power), additional solar cells, batteries, or other energy storage is not required. This has distinct advantages for the mass and power budget of a spacecraft, especially nano and picosats where mass and power are already severely limited. However, unlike other direct energy conversion propulsion technologies (e.g, solar sails), plasmonic
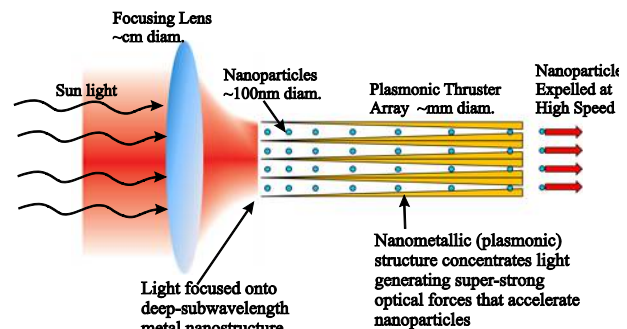
Figure 1: Schematic of plasmonic force propulsion concept.

American Institute of Aeronautics and Astronautics

force propulsion is <u>not</u> due to photon pressure, but rather the strong gradient optical force field setup by surface plasmon polaritons excited in the designed metallic nanostructures by the strongly resonant light-matter interaction. This has distinct advantages in terms of the physical size, mass, and performance of the propulsion system, details of which are provided below. Simulations to predict the strength of the plasmonic force on nanoparticle propellant are described next.

III. Plasmonic Force Predictions

Plasmonic force produced by a three-dimensional nanoscale structure designed to produce a gradient optical force is investigated. A gradient optical force is necessary to expel nanoparticle out of the nanostructures rather than trap them within the nanostructure. First the numerical model used to predict plasmonic force fields and nanostructure transmissions spectra is described. Then the different nanostructures investigated are presented, followed by the results.

A. Numerical Model

Photon momentum is normally too small to have any significant effect, but in nanoscale structures the transfer of linear momentum between light and matter and the associated optical force have been widely studied. Generally, these forces can be divided into scattering and gradient forces, depending on whether the transferred momentum is parallel or perpendicular to the direction of propagation. Optical scattering forces can be used to cool atoms through the interaction with intense laser light. Optical gradient forces are used in optical tweezers, where microscopic dielectric particles are trapped and moved by laser beams towards regions of highest intensity. Recently, optical gradient forces have been investigated in various plasmonic nanostructures, for example, gold nanoparticle dimers and coupled metal planar waveguides. On the basis of plasmonic nanostructures with sub-wavelength mode volume, nanoscale optical tweezers with trapping volume beyond the diffraction limit can also be realized for optical trapping of a single nanoparticle. Besides, surface plasmon polaritons (SPPs) confine the electromagnetic waves into a deep sub-wavelength scale. Such a strong optical confinement results in significantly enhanced optical field strength and gradient of light field. In this case the optical gradient force will be greatly enhanced. In the following content, optical gradient forces have been studied to move and accelerate the nanoparticle in plasmonic nanostructures.

The strong coupling between the nanostructures SPP mode is supported at the interface of the nanostructures and the nanoparticle. The finite-element analysis method (FEM) is used to calculate the optical force of the nanostructure. The asymmetry gold trapezoid structure is designed to generate the giant optical force, which is stimulated by the solar radiation. The nano-scale geometry structure is fixed to get the strongest coupling optical force in solar light wavelength range, based on the TM polarization of the incident light (where the electric field is vertical) and the confined air gap.

The coupling strength determines the optical energy concentration in the gap region, and is related to the gradient optical force generated on the gold nanostructures. This can be calculated by integrating the Maxwell's stress tensor around any arbitrary surface enclosing the nanostructures. The total gradient optical force on the charges in nanoparticle volume V:

$$\boldsymbol{F} = \int_v (\boldsymbol{E} + v \times \boldsymbol{B})\rho d\tau = \int_v (\rho\boldsymbol{E} + \boldsymbol{J} \times \boldsymbol{B})d\tau \tag{1}$$

The force per unit volume is

$$f = \rho\boldsymbol{E} + \boldsymbol{J} \times \boldsymbol{B} \tag{2}$$

eliminating ρ and **J** by using Maxwell's equations:

$$f = \epsilon_0(\boldsymbol{\nabla} \cdot \boldsymbol{E})\boldsymbol{E} + \left(\frac{1}{\mu_0}\boldsymbol{\nabla} \times \boldsymbol{B} - \epsilon_0\frac{\partial \boldsymbol{E}}{\partial t}\right) \times \boldsymbol{B} \tag{3}$$

Now

$$\frac{\partial}{\partial t}(\boldsymbol{E} \times \boldsymbol{B}) = \left(\frac{\partial \boldsymbol{E}}{\partial t} \times \boldsymbol{B}\right) + \left(\boldsymbol{E} \times \frac{\partial \boldsymbol{B}}{\partial t}\right) \tag{4}$$

According to Faraday's laws

$$\frac{\partial \boldsymbol{B}}{\partial t} = -\boldsymbol{\nabla} \times \boldsymbol{E} \tag{5}$$

So

$$\frac{\partial \boldsymbol{E}}{\partial t} \times \boldsymbol{B} = \frac{\partial}{\partial t}(\boldsymbol{E} \times \boldsymbol{B}) + \boldsymbol{E} \times (\boldsymbol{\nabla} \times \boldsymbol{E}) \tag{6}$$

Thus

$$f = \epsilon_0[(\boldsymbol{\nabla} \cdot \boldsymbol{E})\boldsymbol{E} - \boldsymbol{E} \times (\boldsymbol{\nabla} \times \boldsymbol{E})] + \frac{1}{\mu_0}\left[\boldsymbol{B} \times (\boldsymbol{\nabla} \times \boldsymbol{B}) - \epsilon_0\frac{\partial}{\partial t}(\boldsymbol{E} \times \boldsymbol{B})\right] \tag{7}$$

And it can be simplified into the Maxwell stress tensor.

$$T_{ij} \equiv \epsilon_0 \left(E_i E_j - \frac{1}{2}\delta_{ij}E^2 \right) + \frac{1}{\mu_0}\left(B_i B_j - \frac{1}{2}\delta_{ij}B^2 \right) \tag{8}$$

The indices i and j refer to the coordinates *x, y* and *z*. The stress tensor has a total of nine components (T_{xx}, T_{yy}, T_{xz}, T_{yx}, and so on). δ_{ij} is the Kronecker delta. According to Eq. 8, optical gradient force is calculated based on trapezoid nanostructures subjected to the Solar light spectrum from 400 to 1100 nm. Specific nanostructures have been analyzed within the Solar spectrum and are described in the following section.
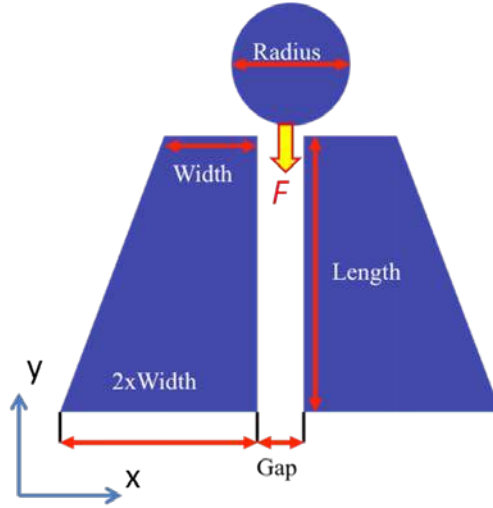
B. Nanostructure Geometry Investigated

Figure 2 shows the schematic of trapezoid structures in 2D views. This asymmetric nanostructure is designed to generate gradient optical electric field in the presence of light within the 400-1100 nm band of Solar light. The FEM is used to calculate the optical force of the nanostructure on the nanoparticle, using Eq. 8. In Figure 2, the incident light is transverse magnetic (TM-) polarization of the incident light (where the electric field is along X-axis). The radius of the glass (silicon dioxide) nanoparticle is 100 nm and is 10 nm above the surface of the nanostructure. The

different nanostructures investigated are shown in Figure 3. All investigated nanostructures are assumed to be gold (Au) nano-trapezoids with a length of 400 nm. Due to the asymmetric structure, the nanoparticle experiences an optical force that is dependent on its position along the Y-axis and move towards the other side of the nanostructure, in the negative Y-direction, as shown in Figure 2. For the desired resonance wavelength, the width of the structures can be tuned so that the strongest optical field concentration inside the metallic structure is acheived. By having nanostructures with different geometry parameters, full Solar spectrum from 400 to 1100 nm can be covered.

Figure 3(a) shows the schematics of asymmetric metallic nanostructures with different geometry parameters. As the width decreases, the nanostructure will support lower resonance wavelength. As one example, Figure 3(b) plots the electric field intensity distributions of asymmetric nanostructure with a width of 100 nm at the resonance wavelength of 800 nm based on our numerical simulation results. Both the 3D view and 2D view are shown in the figure. It is clear that the optical field maximum is located close to the structure end with largest width so that the nanoparticle will be pushed from the end with small width to the other end with large width along the Y-axis. Nanostructures with other geometry parameters supporting different resonance wavelengths have similar optical field distributions.

### C. Transmission Spectra and Force Field Results

Transmission spectrums for the investigated nanostructures are shown in Figure 4. Each nanostructure exhibits a strong resonance within a narrow band (~20 nm) of the Solar spectrum

Figure 2: Schematic of nanoscale asymmetric trapezoid structures in 2D views. The incident light will excite optical resonance of the nanostructure so that gradient optical force will be generated on the nanoparticle (top) and thus the nanoparticle will be accelerated in the negative Y-direction. The arrow shows the direction of the nanoparticle movement.

(Figure 5a). Because of the different dimensions of the nanostructures, each nanostructure resonates at a different wavelength. The four nanostructures investigated have strong resonance at 400, 500, 800, and 1100 nm in the Solar spectrum. The result shows the strong optical resonance from the nano-trapezoid with expected wavelength position, and implies the giant gradient electric field generated within those kinds of nanostructures. The strong optical resonance in the transmission spectrum indicates the strong light confinement and absorption properties. By using nanostructures with different geometry sizes, broadband Solar light from 400 to 1100 nm can be fully used to create strong optical field resonance and therefore gradient optical forces.

Different geometry parameters of trapezoid structures can influence the position of optical resonance wavelength. The width and gap of the nanostructure (as shown in Figure 2) can be used to tune the optical resonance to different wavelengths within the Solar spectrum. The specific dimensions of the investigated nanostructures and their resonant wavelength is listed in Table 1. Resonant wavelength increases from 400 to 1100 nm as the width of the trapezoid structures increases from 40 to 150 nm, while the length is kept constant at 400 nm. The gap size can be tuned from 30 to 50 nm and it has almost no influence on the resonance wavelength of the nanostructure.

American Institute of Aeronautics and Astronautics

The optical force on the nanoparticle as a function of its position along the Y-axis was calculated using Eq. 8 and the results are shown in Figure 5b. The position Y=0 nm corresponds to the center of the nanoparticle at the end of the nanostructure with the narrow width. The particle experiences a positive force that increases to a maximum at the other end of the nanostructure (the widest end) and then decreases as the nanoparticle moves away, out of the nanostructure. At the location of approximately 800 nm out from the nanostructure, the nanoparticle experiences negative optical force which means that the nanoparticle will be slightly decelerated, but will still move outwards because the net force is positive. Since the net optical force over the entire length (from 0 to 1500 nm) is positive, the nanoparticle will move along one direction and eventually be expelled from the nanostructure.
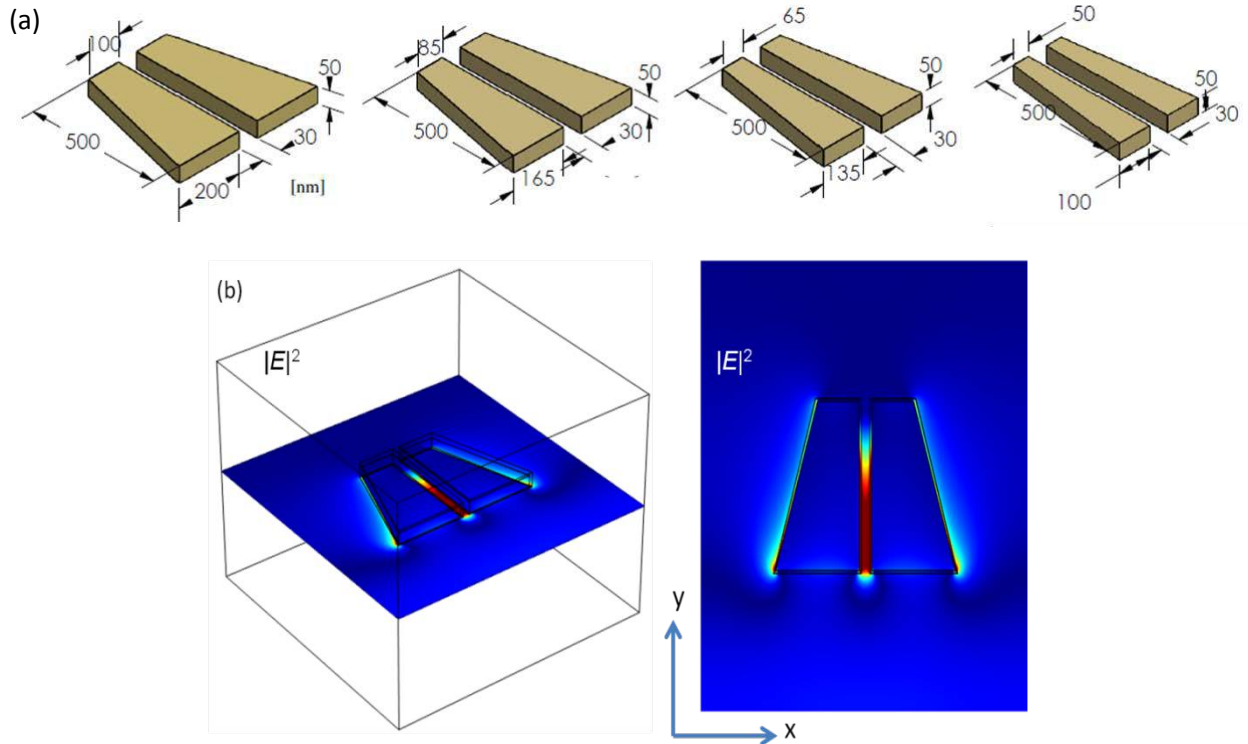
Figure 3: (a) Schematics of asymmetric metallic nanostructures with different geometry parameters. As the width decreases, the nanostructure can support lower resonance wavelength. (b) Asymmetric nanostructures investigated with numerical simulations. The electric field intensity distributions of asymmetric nanostructure with the width of 100 nm at the resonance wavelength of 800 nm are shown. Both the 3D view and 2D view are shown in the figure.

| Resonance wavelength (nm)	Width (nm)	Gap (nm)	Length (nm)
400	40	50	50
500	50	30	30
800	100	30	30
1100	150	30	30

Table 1: Different geometry parameters of trapezoid nanostructures for realizing various resonance wavelengths within the soalr spectrum from 400 nm to 1100 nm. The width of the trapezoid structures is increased to reach longer resonance wavelength. The length of the trapezoid structures are kept at 400 nm.
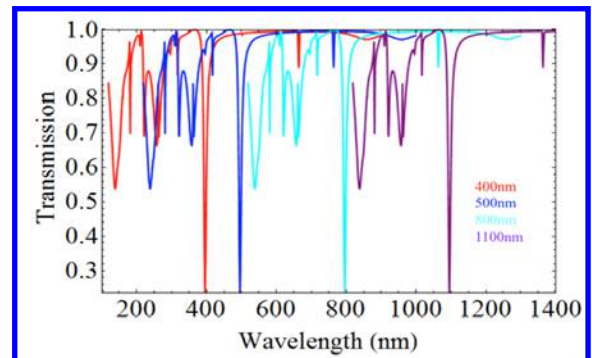
Figure 4: Transmission spectrums of investigated nanostructures in solar light wavelength range from 400 to 1100 nm.

5

American Institute of Aeronautics and Astronautics

The force profile (F(y)) in Figure 5b for each investigated nanostructure is different because of the different resonant wavelength. The broadband Solar spectrum has an irradiance of ~1.85 W/m^2 at 500 nm, and decreases to ~1 W/m^2 at 800 nm (Figure 5a). As the incident solar power decreases, the optical force exerted on the nanoparticle also decreases. Each of the nanostructures investigated will receive a different intensity of light based on where its respective resonance wavelength is located within the Solar spectrum. The largest optical force, which occurs at the end of the trapezoid structure, increases from 20 pN/W to 65 pN/W as the nanostructure resonant wavelength decreases from 1100 to 500 nm. While the largest optical force decreases from 65 pN/W to 45 pN/W as the resonant wavelength decreases from 500 to 400 nm. Again, these optical force trends are due to the relative optical intensity across the solar spectrum showing a blackbody emission from the Sun with the peak optical intensity at ~500 nm (Figure 5a). The result shows that the optical gradient force can accelerate the nanoparticle along Y-axis in nano-trapezoid structure, and is a promising technology to be harnessed for the propulsion of nano-satellites.
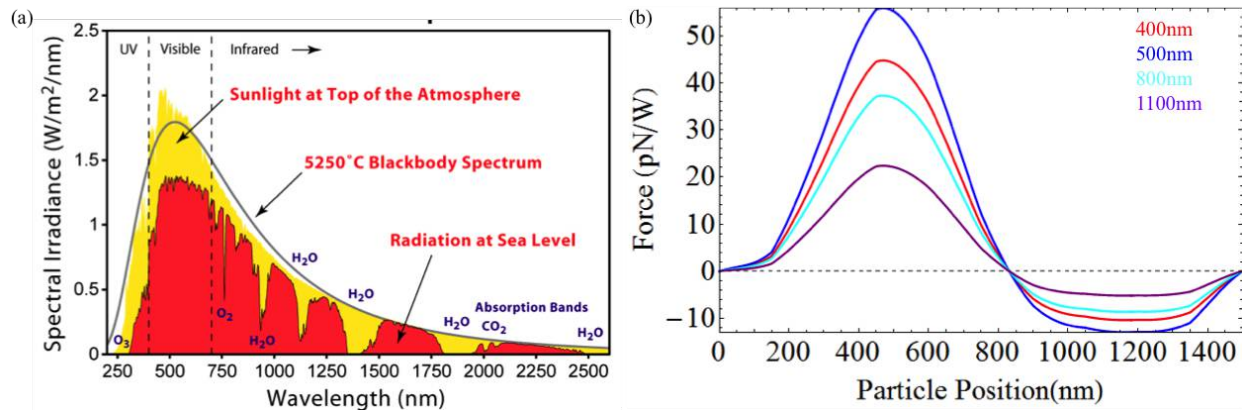

Figure 5: (a) Solar radiation spectrum; (b) The calculated optical forces exerted on the nanoparticle at different resonance wavelength of 400, 500, 800, and 1100 nm within the Solar spectrum.

IV.   Plasmonic Propulsion Performance Predictions

Nanostructure force profiles shown above were used in an analytical propulsion performance model to predict the thrust and specific impulse of a plasmonic force thruster. Specifically, results were used to develop a conceptual plasmonic force thruster. The impact of important thruster design variables, such as nanoparticle size and mass, nanoparticle exhaust rate, nanostructure array size, and incident power, are presented here.

A.   Conceptual Design of a Plasmonic Propulsion Thruster

The general conceptual design of a plasmonic propulsion thruster, based on the knowledge gained from nanostructure simulations, is shown in Figure 6. It is a layered multi-stage array of nanostructures. Multiple nanostructures must be placed end-to-end (in series, a multi-stage geometry) in order to provide an appreciable acceleration of the nanoparticle propellant. This is the multi-stage length, and also the acceleration length, L. A layered structure is beneficial for efficient use of solar light. Nanostructures on top resonate with shorter wavelengths of the solar spectrum, while the longer wavelengths pass through to resonate with deeper layers. A structure with 4 layers is shown in the figure below, but transmission spectra results (Figure 4) show that the absorption/resonant band is very narrow (~20 nm) for a particular nanostructure. This means that many more layers can be used and the
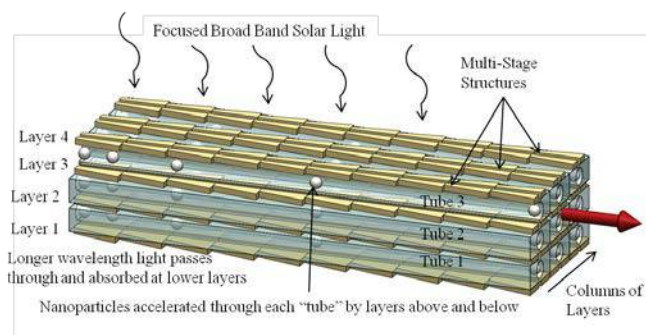
Figure 6:   Illustration of a plasmonic force thruster. Incident focused broad band solar light resonates with each layer of nanostructures. Longer wavelengths are absorbed (resonate) with deeper layers. In between each nanostructure layer are nanoparticle guide tubes. Nanoparticle propellant is accelerated and expelled from the guide tube by the combination of forces from the nanostructure layers above and below it.

6
American Institute of Aeronautics and Astronautics

following analysis assumes 36 layers each with a 20 nm resonance band within the 400-1100 nm solar broadband. In between each layer is a nanoparticle guide tube. Nanoparticle propellant is accelerated and expelled from the guide tube by plasmonic forces applied from the nanostructure layers directly above and below it. The following analysis assumes there are 36 layers of nanostructures with 35 guide tubes in between. This layered multi-stage structure is repeated (columns) to form a large array of N elements, where N = layers (rows) x columns. The area solar light is incident upon is the thruster area, $A_{thruster}$, and is the acceleration length, L, times the number of columns in the array. Not shown in Figure 6 is the solar light focusing lens.

B. Analytical Propulsion Performance Model

The performance of a plasmonic thruster was analytically modeled based on the design parameters of the conceptual model shown in Figure 6. Specifically, both thrust and specific impulse are predicted using fundamental physics models. Solar light power incident on the thruster is dependent on the focusing lens diameter (area, A_{lens}) as shown in Eqn. 9, where I is Solar intensity in low-Earth orbit (1.4 kW/m^2). The Solar light power incident on a single nanostructure that makes up the thruster array is given by Eqn. 10. It is clear from this relationship that maximizing the collection lens size and minimizing the thruster area increases the power incident on each individual nanostructure, which increases the accelerating plasmonic force on the nanoparticle propellant (Figure 5b).
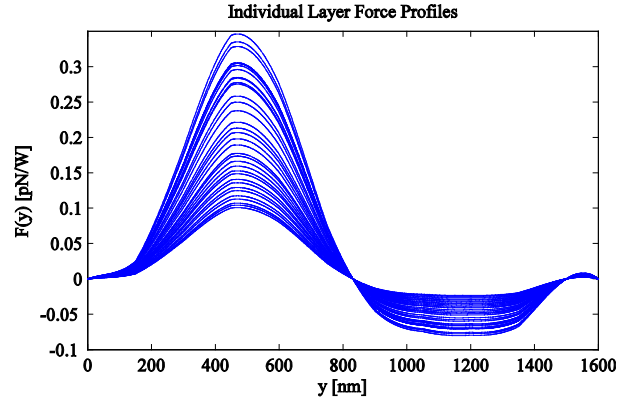
$$P_{thruster} = IA_{lens} \tag{9}$$

$$P_{nanostructure} = P_{thruster} \frac{A_{nanostructure}}{A_{thruster}} = I \frac{A_{lens} A_{nanostructure}}{A_{thruster}} \tag{10}$$

Incident Solar light excites SPPs in each nanostructure of the thruster array, resulting in an optical force on the nanoparticle propellant as given by Figure 5b. The force is a function of position within each individual nanostructure, and is therefore a function of position along the entire multi-stage series of nanostructures, F(y). The force profile for an individual nanostructure is given by the results of the electrodynamic simulations shown in Figure 5b. This single nanostructure force profile is assumed to be the same for each nanostructure constituting the entire multi-stage assembly of nanostructures. Additionally, the force profile is different for each layer of the multi-stage geometry. That is, each layer has a nanostructure with different dimensions to resonant with a different desired bandwidth of the solar spectrum, and, as a result of the relative intensity across the solar spectrum and the efficiency of

Figure 7: Optical (plasmonic) force applied to a 100 nm nanoparticle for each of the 36 layers of the conceptual plasmonic thrusters.

different nanostructure geometry, the force profile is different for each layer, as shown in Figure 5b. For example, at 500 nm, the solar broadband has an intensity of ~1.85 W/m^2, whereas at 800 nm, it is ~1.14 W/m^2. We extrapolate the results for all 36 layers based on the results from the four nanostructures simulated above, results shown in Figure 5b. The extrapolated results across all 36 layers are shown in Figure 7.

The final velocity of the nanoparticle propellant is calculated using Eqn. 11, where v_i is the final velocity (assuming zero initial velocity) of the nanoparticle out of tube i, $F_{above,below}(y)$ is the force profile associated with the multi-stage nanostructure layer above or below the nanoparticle guide tube, L is the length of the multi-stage nanostructure, and m is the mass of the nanoparticle. Each layer of the thruster is expelling nanoparticles at different velocity because the plasmonic force on the nanoparticle is different for each nanostructure geometry.

$$\frac{v_i^2}{2} = \int_0^L \frac{F_{above}(y) + F_{below}(y)}{m} dy \tag{11}$$

American Institute of Aeronautics and Astronautics

The total thrust force (T) of the thruster array is the sum of the thrust produced by each individual tube expelling nanoparticles. Each layer is expelling nanoparticles at different velocity, but the model assumes each tube is expelling nanoparticles with the same mass, m, and at the same rate, f. The thrust can be calculated using Eq. 12 below, where N is the number of guide tubes in the array (the size of the array) and f is the rate at which the nanoparticles are being expelled from each tube (sec^{-1}). Specific impulse (I_{sp}) is calculated using Eqn. 13, where $g_0 = 9.81$ m/s^2.

$$T = \sum_i^N \dot{m} v_i = \sum_i^N m f v_i \qquad (12)$$

$$I_{sp} = \frac{T}{\dot{m} g_0} = \frac{T}{N m f g_0} \qquad (13)$$

C. Propulsion Performance Results

The following sections describe results from the propulsion performance model. Specifically, the effects of particle mass (size and density, $m = \rho V$), acceleration length, L, expulsion rate, f, array size, N, and collection lens size, A$_{lens}$, on propulsion performance (T, I$_{sp}$) are investigated.

Figure 8: Comparison of the mass of the possible nanoparticle propellants with variation in particle diameter

Preliminary analysis using representative force profile data offers a good basis to determine how the key performance characteristics will depend on the constraints of the plasmonic simulations, as well as characteristics of the nanoparticle. Thrust force and specific impulse directly depend on the mass, and thus implicitly the density and size of the nanoparticle being expelled. Gold, glass, and polystyrene nanoparticles are investigated because these are commonly used in nano-optics and plasmonic experiments. Figure 8 shows a comparison of nanoparticle mass relative to size (diameter) of the particles.

The effect of nanoparticle type and size on propulsion performance is shown in Figure 9. The analysis assumes a 5 mm acceleration length (L), particle expulsion rate (f) of 1x10^6, array size (N) of ~3000 (35x86) 'tube' sections, and a 5 cm diameter focusing lens (A$_{lens}$). The feasibility of these parameters is discussed in a following section. Results show that thrust increases while specific impulse decreases as the nanoparticle diameter increases. The lighter polystyrene nanoparticles have higher specific impulse but correspondingly lower thrust.
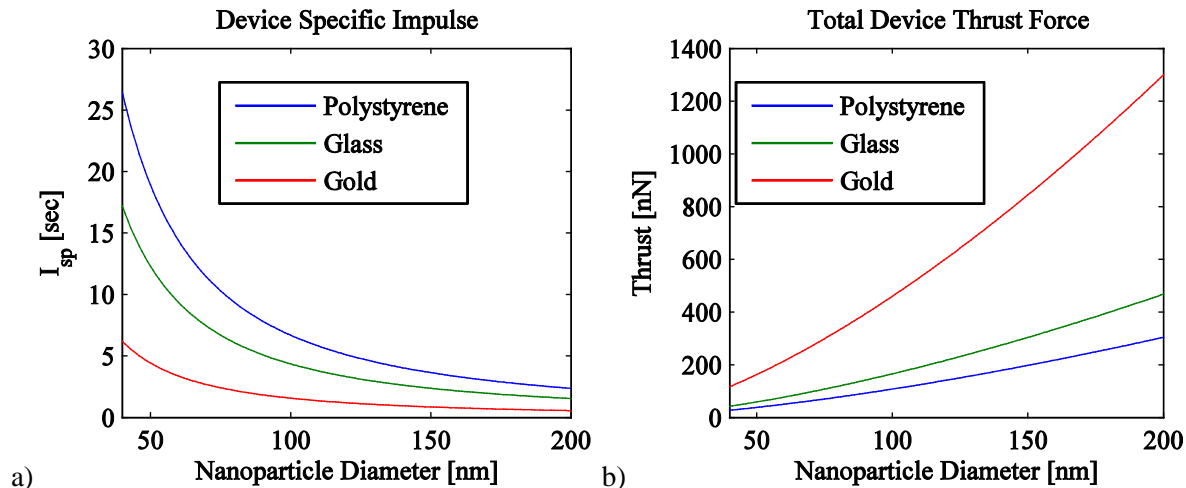

Figure 9: Performance analysis of the conceptual plasmonic thruster, calculated using a 5 mm acceleration length in an 86 by 36 layer thruster array. (a) Comparison of the specific impulse and (b) thrust of each nanoparticle propellant.
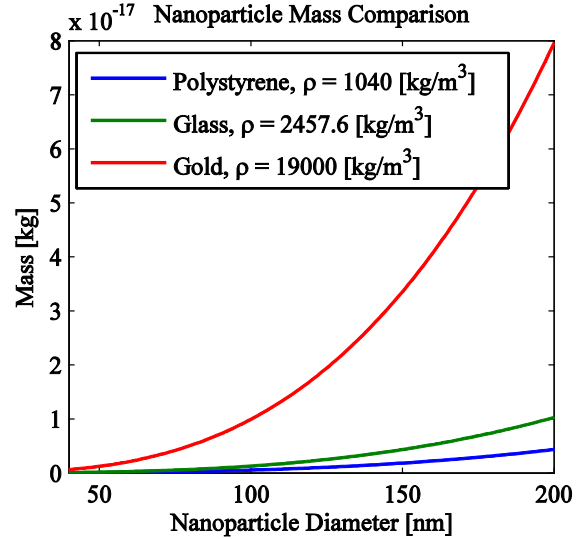
Increasing the acceleration length (L) does not increase the thrust or specific impulse. A longer acceleration length does increase the thrust and the specific impulse for a constant incident light power, as shown in Eqn. 11. But as acceleration length increases, the total area of the nanostructure array (i.e., $A_{thruster}$) also increases. As Eqn. 10 shows, this will reduce the power incident on the thruster, resulting in decreased plasmonic force. The increase provided by longer acceleration length is cancelled by the decrease in light power incident on the thruster.

An identical trend is found for the array size (N). Increasing the array size (N) does not increase the thrust. Array size also has no impact on specific impulse. A larger array size would increase thrust for a constant incident light power, as shown in Eqn. 12. But as array size increases, the total area of the nanostructure array

Figure 10: Specific impulse and thrust vs. lens diameter for 100 nm polystyrene nanoparticles.

(i.e., $A_{thruster}$) also increases. As Eqn. 10 shows, this reduces the power incident on the thruster, resulting in decreased plasmonic force. The increase provided by a larger array is cancelled by the decrease in light power incident on the thruster.

Expulsion rate (f) does directly impact the thrust, but has no impact on specific impulse, as shown in Eqn. 12 and 13. Thrust increases linearly with expulsion rate. Specific impulse is a measure of the exit velocity, and the rate at which particles are being expelled does not effect their final velocity. Expulsion rate is estimated to be 1×10^6 per second for the analysis here, based on previous studies of nanoparticle extraction using gas jets [8].

Thrust and specific impulse are greatly affected by the light power incident on the nanostructures. That is, by the size of the collection lens used to focus solar light onto the thruster, A_{lens}. There is a linear relationship between lens diameter and thrust and specific impulse, as shown in Figure 10. This is a direct result of Eqn. 10, where the lens area directly increases the incident power on the thruster, which increases the plasmonic force, total nanoparticle acceleration, exit velocity, specific impulse, and thrust. The relationship is linear because of the proportionalities in the above equations, which is summarized here. The solar power incident on the thruster is proportional to the lens area, which is proportional to the square of the lens diameter (Eqn. 10). The power incident on the thruster is also proprtional to the plasmonic force generated by the the nanostructures, which is proportional to the square of the exit velocity (Eqn. 11) and square of the specific impulse and thrust (Eqn. 12 and 13). Therefore lens diameter should be linearly related to the thrust and specific impulse, which is what the model results show (Figure 10).

V.   Position and Pointing Precision Capability

Propulsion performance results in the above section are used to evaluate position control resolution and pointing precision of plasmonic force propulsion for nano/pico-satellites. Attitude control simulations using a bang-bang control algorithm are used to compare different types of thrusters and torquers for small spacecraft.

A. Bang-Bang Control Algorithm and CubeSat ACS Model

Three separate programs were written in MATLAB to simulate three different control scenarios; attitude control using RCS thrusters, proximity control using RCS thrusters, and attitude control using reaction wheels. Each of these scenarios assumes a cubeSat employing a *bang bang* or "On/Off" control algorithm to move to or maintain a desired position or attitude in the presence of Solar Radiation Pressure (SRP).

The algoriothms for each code is as follows. The user inputs mass and size of a cubeSat, as well as the thruster moment arm, thrust, number of thrusters, specific impulse, and the switching time of the thruster to be tested. The worst case scenario solar radiation torque or force is calculated using the cubeSat size as described in a following section. The user then defines an initial attitude/position, initial velocity, a desired attitude/position, and switching interval. The body of the code is a "for" loop where each iteration calculates the satellite current position or attitude, and is illustrated by the flow chart in Figure 11. In each iteration the thruster is either on or off for the switching time of the thruster. The simulation keeps track of the spacecraft attitude/position and velocity, and decides whether or not it is necessary to fire the thruster and in which direction the thruster should be fired to keep the satellite at the desired attitude/position. It is assumed that the satellite sensors measure the attitude/position and the angular velocity/linear velocity with zero error. If the current attitude/position is outside of the switching interval then the
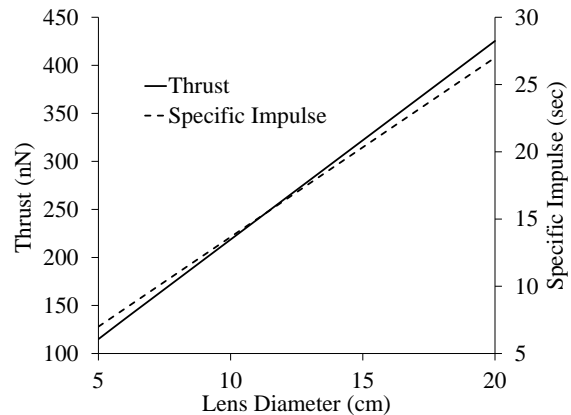
9

spacecraft fires its thrusters in the appropriate direction to arrive at the set attitude/position. The spacecraft constantly calculates the distance it will take to stop if it decelerated constantly from its current velocity to zero. When that distance equals the distance away from the set attitude/position the spacecraft will decelerate to zero velocity. If the attitude/position is inside the switching interval the spacecraft measures its velocity. If the velocity is greater than the smallest change in velocity the thrusters are capable of producing and the velocity and pointing error are both positive or both negative (meaning the attitude vector is moving away from the desired attitude) then the thrusters will fire in order to nudge the spacecraft back toward the desired position/attitude.

Throughout the simulation the current attitude/position, velocity, torque/force, and propellant consumption are recorded and plotted. If the thruster is not capable of keeping the attitude/position of the satellite within 10% of the switching interval a warning is displayed stating that the current thruster is not capable of maintaining the switching interval desired.
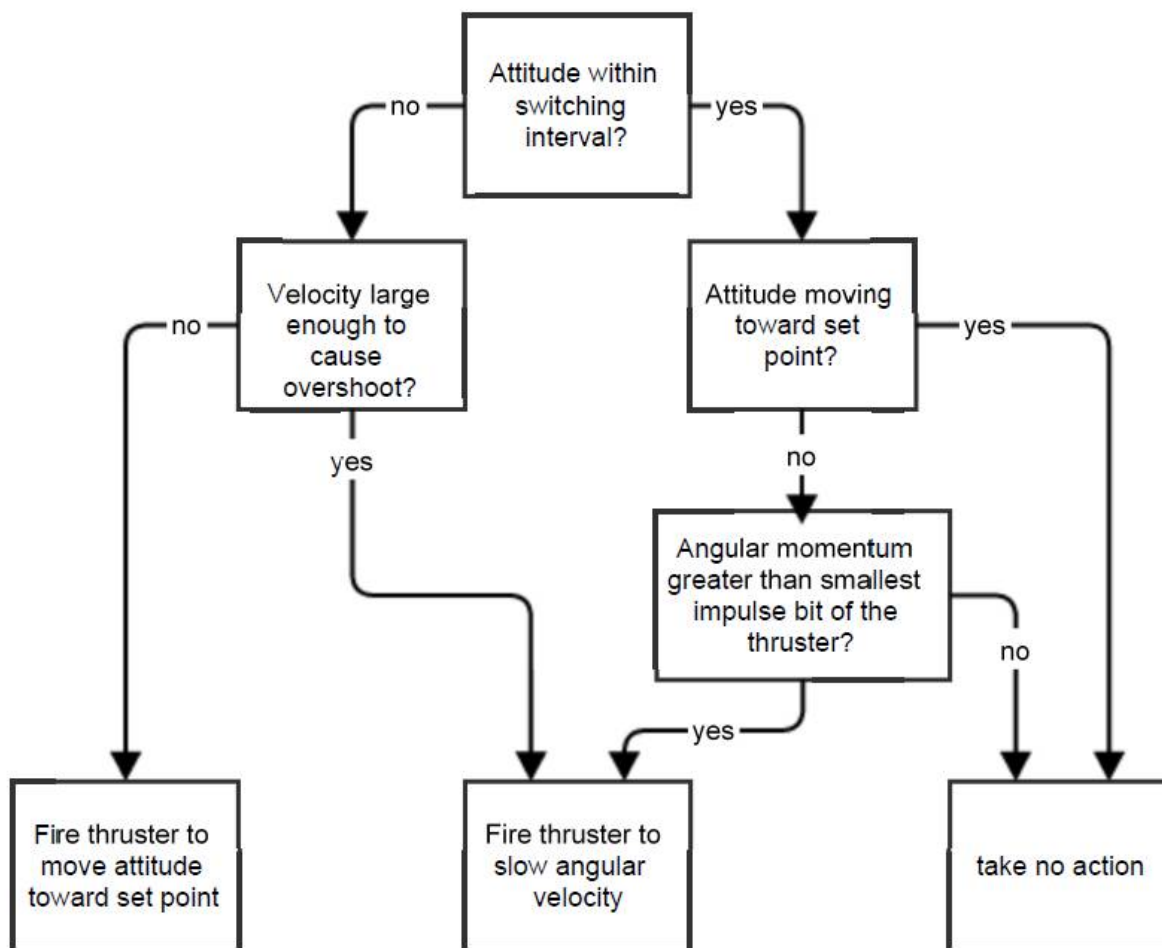
Figure 11: Flow chart outlining the bang-bang control algorithm used for attitude control. The same flow chart can used for proximity control by simply replacing the words attitude, angular momentum, and angular velocity with position, momentum, and velocity, respectively.

This section describes in detail the mathematical model used to model position control using RCS thrusters. The assumptions of this model are as follows:
1. There are no outside forces affecting the motion of the spacecraft other than its thrusters and solar radiation pressure.
2. This is a single axis simulation so all forces (thrust and SRP) act only along that axis.
3. The spacecraft always knows its current position and velocity with perfect accuracy.
4. The point/object/other satellite which the spacecraft is trying to maintain proximity to is inertially fixed.

American Institute of Aeronautics and Astronautics

5. SRP is constant and is calculated for the worst case scenario where the Sun is directly behind the spacecraft and the spacecraft surfaces reflect light perfectly back toward the Sun.
6. The attitude of the spacecraft remains constant such that one face of the cubeSat is directly facing the Sun.
7. The spacecraft is a cube with constant density.
8. For every time step of the simulation the thrusters can either be fired or not fired. There is no recharge time for the thrusters and each burst delivers the exact same impulse bit for the specified switching time.
9. Because fuel consumed during simulations is very small (usually less than 1 mg) the spacecraft is assumed to have constant mass.

Spacecraft inputs are its mass, M in kg, and the length of a side of the cubeSat, L in m. Thruster inputs are thrust, F in N, switching time, t in s, specific impulse, Isp in seconds, number of thrusters, n, and the mass of on board propellant, Mp in kg. The spacecraft is assumed to be under constant acceleration from SRP. For a 1U cubeSat with one face directly facing the Sun the force due to SRP = 90.6 nN. The acceleration due to solar radiation and due to the thrusters being fired is easily calculated using Newtons second law.

After initializing the position, velocity and desired position, the simulation begins. Each iteration represents a time step lasting for the switching time t. During each iteration the bang-bang algorithm decides whether to fire the thrusters in the +x direction or the -x or to take no action. Also, each iteration the distance required for the spacecraft to stop at its current velocity is calculated using the basic kinematic equations found in any elementary physics text [9-10].

$$x_{stop} = \frac{1}{2}\frac{V^2}{a_{thrust}}$$ (14)

In the case where the spacecraft is outside of the switching interval but moving toward the desired position this result is used to decide whether the thrusters should continue firing toward the desired position or fire the opposite direction bringing the spacecraft to a stop. After deciding whether or not to fire the thrusters and in what direction the current position and velocity of the spacecraft are updated.

$$x_{new} = x_{old} + \frac{1}{2}a_{thrust}t^2 + \frac{1}{2}a_{SRP}t^2 + V_{old}t$$ (15)
$$V_{new} = V_{old} + a_{thrust}t + a_{SRP}t$$ (16)

where $a_{thrust} = +/-nF/M$ or 0 depending on whether or not the thrusters are being fired and in which direction. Finally the total time the thrusters have been operating, T is recorded and the mass of propellant which has been expended, M_e is calculated using [11]

$$M_e = \frac{nFT}{gI_{sp}}$$ (17)

Plots of the spacecraft's position and velocity, as well as the force produced by the thrusters, the error in the position and velocity, and the propellant consumed are produced. A sample output of the simulation is provided in Figure 12. The sample output shown was generated simulating a 2 kg 1U cubeSat with two PFP thrusters producing 250 nN of thrust with a switching time of 1 ms. The cubeSat moved 10^{-10} m then held position within a switching interval of 2×10^{-12} m, all while under a 90 nN disturbance force from SRP.

A similar model is used to simulate attitude control using RCS thrusters. In this case angular motion is modeled instead of linear motion. Results similar to those shown in Figure 12 are obtained for angular motion. A sample output of the attitude control simulation is shown in Figure 13, showing how the spacecraft attitude, and angular velocity vary with time as well as when the thrusters fire and the propellant usage. The simulation shown was generated simulating two PFP thrusters mounted on either side of a 2 kg 1U cubeSat scaled such that their thrust was only 50 nN. The thrusters also had a specific impulse of 2.9 s, and a switching time of 1 ms. The cubeSat rotated a distance of 5×10^{-8} degrees which is 1.8×10^{-4} arc-seconds then came to a stop and maintained a switching interval of 1×10^{-9} degrees or 3.6×10^{-6} arc-seconds in the presence of SRP. The solar radiation torque was pushing the cubeSat in the $+\hat{\theta}$ direction which is what caused it to overshoot as it approached the set attitude of zero degrees. For more details on the proximity and attitude control simulations the reader is referred to Ref. [12].
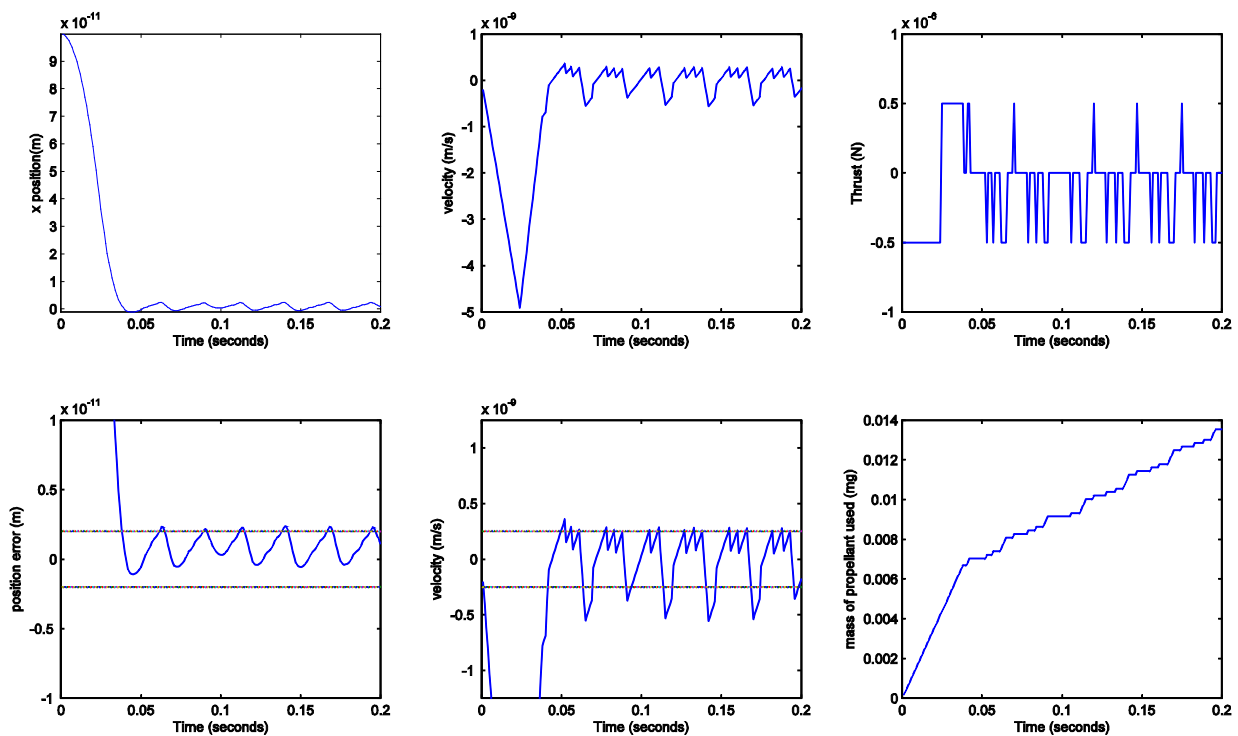
Figure 12: Sample output of proximity control simulation.
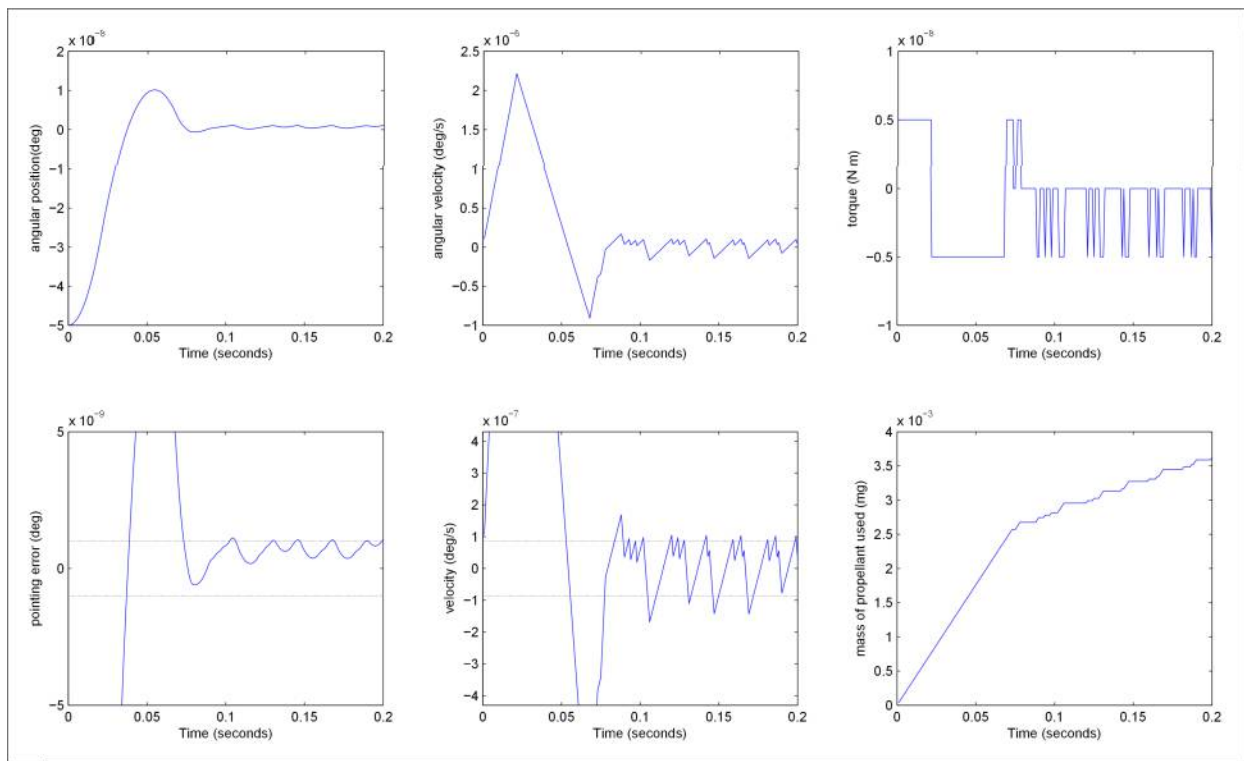
Figure 13: Sample output of attitude control simulation.

B. Position and Pointing Comparison of Different Thrusters and Torquers

Several new and developing micro propulsion systems for small satellites were studied and modeled using the algorithms presented in the section above. This section documents the characteristics of each thruster system and compares its performance to that of plasmonic force thrusters. The results of the simulations and a comparison of the characteristics of each thruster is summarized in the last part of this section.

1. Plasmonic Force Propulsion (PFP) Thrusters

The size, configuration, and propellant type of PFP thrusters will be easily customizable to fit the needs of various missions. In this study a single thruster configuration consisting of an array of 3010 (35x86) devices, 5 mm long acceleration length, with each tube expelling 1×10^6 100 nm diameter polystyrene nanoparticles per second was used to obtain baseline thrust and specific impulse estimates. This baseline thruster is 35 nanotubes thick and 86 wide, on the top and bottom of each nanotube is a plasmonic nanostructure each designed to resonate with a different wavelength of light ranging from 400 to 1100 nm. Such a thruster would have a width of 52 μm and a thickness of 5 μm. By comparison a human hair is 70 μm in diameter. The mass of each thruster would be negligible so the system mass would be determined by the 5-cm-diameter lens used to focus the light on the nanostructures and the total mass of the propellant used. It is estimated that such a multistage array plasmonic thruster with all the light from a 5 cm diameter lens focused on it would have a thrust of 107.5 nN and a specific impulse of 6.69 s.

The switching time of PFP thrusters is currently not known and will be determined by how the thruster is actuated. Actuation of the thruster could be controlled by a mechanical shutter or electric glass allowing light to shine on the nanostructures, or an electronically controlled valve on the nanoparticle propellant tank or a combination of these. A mechanical shutter would allow for very fast switching times, high end cameras typically have shutter speeds higher than 1/10,000 of a second. However, the vibrations from a shutter could induce unwanted motion in the spacecraft. Electric glass using "micro-blinds" can change from opaque to transparent and back on the order of a millisecond but is still under development.[13]

2. Micro-Cathode Arc Thrusters (μCAT)

The Micro-Cathode Arc Thruster (μCAT) is currently under development at The George Washington University and is at TRL-4. The μCAT consists of a titanium cathode and a copper anode separated by an insulator. The copper anode is surrounded by an inductor which releases a high voltage pulse causing a discharge between the electrodes. The titanium cathode acts as the propellant and ablates during the discharge as a portion its surface is converted to plasma. The plasma is then accelerated out of the thruster being directed by the magnetic field of the inductor.[14-16]

The main advantages of the μCAT is that it has high I_{sp} (2000-3500 s), relatively high thrust (100 μN), and low mass (100 g per thruster) [14],[16]. A cubeSat using μCAT thrusters would also require a inductive pulsed power unit adding a mass of approximately 100 g. The titanium cathode acting as propellant has a mass of 40 g and density of 4.5 g/cm^3. Assuming that the entire titanium cathode is consumed as propellant, a 2 kg cubeSat equipped with a μCAT would have 400-700 m/s of ΔV meaning that the cubeSat would be able to easily perform orbital maneuvers besides station keeping. However, the μCAT is currently only estimated to have a lifetime of 10^8 pulses, meaning with an impulse bit of 2 μNs, it will only be able to provide 100 m/s of ΔV to a 2 kg cubeSat. [17] With a switching time of 20 ms the μCAT can provide good pointing and positioning accuracy of 1×10^{-4} deg and 6×10^{-4} m. As a result of the relatively high thrust produced by the μCAT and larger switching time it is not as well suited for missions which require high accuracy pointing and proximity control as PFP thrusters.

3. Vacuum Arc Thrusters (VAT)

The Vacuum Arc Thruster (VAT) developed by Alameda Applied Sciences Corporation uses a solid metal cathode as the propellant and is considered to be at TRL-5. A vacuum arc is an electric discharge which occurs in a vacuum between a heated cathode and an anode containing the solid metal propellant. A large number of metals are available as propellants including titanium, yttrium, silver, tantalum, and tungsten, but the two most common are titanium and tungsten having densities of 4.5 g/cm^3 and 19.25 g/cm^3, respectively. Typically VATs use a 40 g titanium anode as the propellant. As the electron beam strikes the propellant anode its surface becomes a plasma which is then accelerated away from the thruster at high speed.[18-21] The VAT has an extremely large throttleable average thrust range of 10 nN to 300 μN a high specific impulse of 1000-3000 s and a fast switching time of 1 ms. The average thrust ranges from 10 nN to 300 μN, but this is done by altering the switching time of the thruster. The range of impulse bits is 10 nNs to 30μNs. Thus the lowest instantaneous thrust assuming a 1 ms switching time is 10 μN.[18]

With the combination of a wide range of throttleable thrusts and a fast switching time of 1 ms the VAT can maintain extremely low switching intervals. If used on a 2 kg cubeSat it could provide precision pointing to 2×10^{-7} degrees and position accuracy up to 4×10^{-11} m. With its high specific impulse it could provide 200-600 m/s of ΔV assuming it consumed the entire titanium anode as propellant. However, the rated lifetime of the VAT is only 5 million pulses so each VAT is only able to provide 75 m/s of ΔV to a 2 kg cubeSat. In addition to this the VATs 300 g PPU requires 10 W of power to operate.

The main advantages of the VAT are its large throttleable thrust range, low minimum impulse bit, and fast switching time which allow for extremely low switching intervals at the limit of what a cubeSat can sense. However, its relatively short lifetime, high power consumption, and relatively large mass limit its utility on cubeSats.

4. Pulsed Plasma Thruster (PPT)

PPTs were originally developed in the late 1960's and were the first successful electric propulsion system used in space. They are easily scalable and have been used on a number of large satellites as both an ACS and RCS. PPTs commonly use solid PTFE (teflon) as a propellant. The teflon is ablated and converted to plasma through a high voltage electric discharge between two capacitor plates. the plasma is then accelerated away via the Lorentz force. [22]

Clyde Space makes a small electric propulsion system for small satellites called the Pulsed Plasma Thruster (PPT), which produces a thrust of 4.5 μN, has a switching time of 0.2 s, and a specific impulse of 608 s. The thruster with all supporting systems comes in a $90 \times 90 \times 27$ mm envelope which conveniently fits into the back fourth of a 1U cubeSat.[23] It carries 7 g of teflon propellant the density of which is 2.2 g/cm^3, which provides 21 m/s of ΔV for a 2 kg cubeSat. The thruster has a lifetime of 1.5 million pulses and is estimated to provide 42 N-s of total impulse. Currently there is no PPT designed to be used as an ACS on cubeSats and is primarily suited for extending the mission life of cubeSats by providing a small amount of ΔV to combat atmospheric drag. The main advantage of PPTs is that they are a flight proven technology, but they are not as small and efficient as newer thruster systems.

5. Electrospray Thrusters

Electrospray thrusters operate by accelerating electrically charged droplets of ionic liquids at high speeds using high voltage electric fields. Various electrospray thruster designs vary widely and are constantly being improved. They have previously been used on larger satellites but MIT is currently developing a miniaturized version for use on cubeSats. Electrospray thrusters have a number of advantages such as high thrust (100 μN), high specific impulse (2500-5000 s), and have a short switching time (1 ms). Each thruster is very small, about the size of a penny, and is only a few grams. an exact mass estimate is not available since the thruster is still under development but each one should have a mass under 10 g. Their main disadvantages are that they require a large high voltage power processing unit which draws 10 W of power, occupies a volume of 300 cm^3 and adds 250-300 g to the system mass. MITs miniature electrospray thrusters are expected to have an extremely long life and should give cubeSats relatively large amounts of ΔV. They will also provide both positioning and attitude control but not to the level of precision of PFP thrusters. [24-27]

6. Reaction Wheels

Currently there are not many cubeSat reaction wheels available but a new model which came out in the past year is the Blue Canyon Technologies Micro Reaction Wheel. It has a moment of inertia of 28.6×10^{-6} kg·m^2, mass of 150 g, volume of 33 cm^3, and a max torque of 0.6 mN-m. It only requires a maximum of 1 W of power and operates from 5-15 V. The wheel can reach a maximum speed of 6,000 RPM, and is expected to have a lifetime of 3 years. [28] For the purposes of the simulation it was assumed that the reaction wheel had a reaction time of 0.1 s. This gave a pointing accuracy of 0.01 degrees when placed on a cubeSat. Because of the large torques reaction wheels are able to provide they can turn a cubeSat much quicker than micropropulsion thrusters, however, they do not provide as fine of pointing accuracies.

7. Micropropulsion summary

Table 1 compares the characteristics of all the micropropulsion systems and reaction wheels considered in this study. These results are also presented in Figure 14. As many of these thrusters are still in development and/or easily customizable the values presented in this table vary from source to source.

Table 2: Comparison of various cubeSat propulsion systems.

Thruster type	PFP	μCAT	VAT	PPT	Electrospray	Reaction Wheels
Thrust used in Simulations	250 nN	100 μN	10 μN	4.5 μN	100 μN	N/A
Specific Impulse (s)	1-12	2000-3500	1000-3000	608	2500-5000	N/A
Switching Time (ms)	1	20	1	200	1	100
Pointing Accuracy (deg)	2×10^{-9}	1×10^{-4}	2×10^{-7}	N/A	1×10^{-6}	0.01
Position Accuracy (m)	3×10^{-12}	6×10^{-8}	4×10^{-11}	8×10^{-7}	6×10^{-10}	N/A
Min Impulse Bit (nNs)	50 pNs	2 μNs	10 nNs	900 nNs	100 nNs	N/A
Thruster Mass (g)	<0.001	100	90	280	<10	N/A
Supporting Systems Mass (g)	100	100	300	0	250	150
System Volume (cm^3)	50	200	200	220	300	33
Propellant Mass (g)	50-100	40	40	7	20	N/A
Propellant type	Nanoparticles	Metal (Ti)	Metal (Ti or W)	Teflon	Ionic Liquids	N/A
Propellant Density (g/cm^3)	1.04	4.5	4.5	2.2	varies	N/A
Max Power Required (W)	0	5	10	2.7	10	1
ΔV for 2kg cubeSat (m/s)	1-6	~100	~75	21	250-500	N/A
Lifetime (pulses)	unknown	10^8	5×10^6	1.5×10^6	unknown	three years
Configurable as ACS?	yes	yes	yes	no	yes	yes
Scalable/Customizable?	yes	yes	yes	no	yes	yes
Throttleable?	yes	no	yes	no	yes	yes
High Voltage Required?	no	yes	yes	yes	yes	no
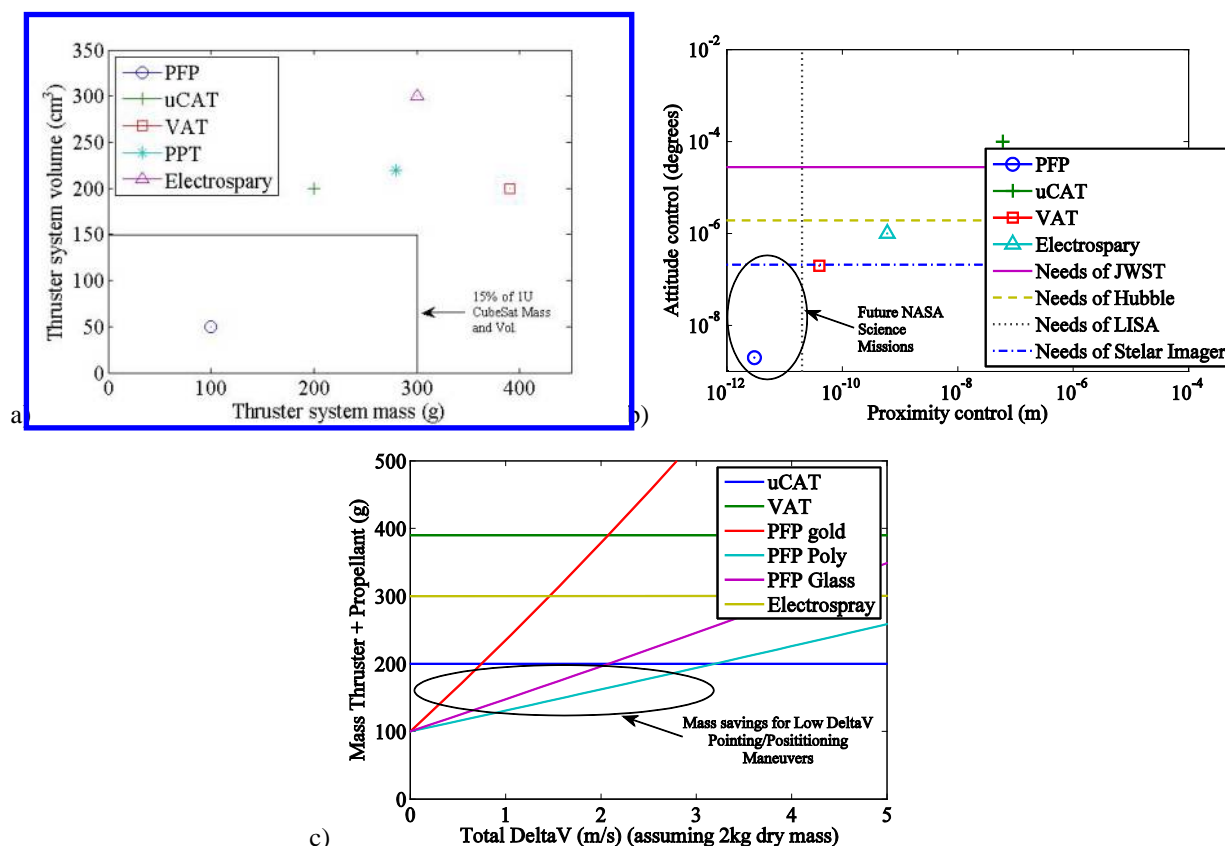
Figure 14: Comparison of plasmonic force propulsion with other state-of-the-art thruster systems. a) Thruster system mass and volume, b) proximity and attitude control capability in comparison with various relevant NASA missions, and c) thruster and propellant mass as a function of total delta-V for a 2 kg dry mass spacecraft.

From our analysis it is clear that plasmonic force propulsion can extend spacecraft pointing and precision control into an entirely new realm. Figure 14 compares PFP with the other types of propulsion investigated. Thruster system mass is 50% smaller and volume is 75% smaller (Figure 14a). While at the same time, PFP can provide attitude control that is over two orders of magnitude more precise (10^{-9} vs. 10^{-7} degrees, or 0.007 vs. 0.7 milliarcseconds) (Figure 14b). Additionally, PFP can provide proximity control that is an order of magnitude more precise (10^{-12} vs. 10^{-11} m), such that the limiting factor becomes the interferometer used to measure the distance between the objects. PFP enables new types of missions that require this ultra-precise level of pointing precision, such as the Stellar Imager (Figure 14b), and proximity control precision, such as LISA (Figure 14b). Finally, it is clear that PFP is beneficial for pointing and proximity control operations that require relatively low delta-V (i.e., not main propulsion for orbit raising where high delta-V is required) (Figure 14c). For low-delta-V maneuvers, like for the Stellar Imager (delta-V of mm/s), PFP is ideally suited. In fact, for total mission delta-V of about 3 m/s or less, PFP propulsion saves mass over competing propulsion systems.

The ultra low thrust of PFP thrusters could also be used for attitude or proximity control on larger satellites. NASA's Laser Interferometer Space Antenna (LISA) mission to detect gravitational waves requires that the satellites know their positions relative to each other and maintain precise orbits to with respect to each other. The LISA spacecraft will not be formation flying and the distance between them will be constantly changing but needs to be constantly known to within 20 pm over 5,000,000 km. As a result, this mission will require extremely precise reaction control thrusters with thrusts on the order of a micro-newton or less.[29-31] PFP thrusters can position a cubeSat accurately to within 3 pm, meaning they could position a larger satellite with greater precision making them a viable option for the LISA mission or future NASA missions which require greater precision.

PFP thrusters are also a viable option for the NASA proposed Stellar Imager or SI mission[††]. This mission concept consists of 20-30 formation flying "mirror sats" each one a meter diameter mirror precisely placed to within 5 nm over several kilometers. Each mirror sat will also have to control its attitude to less than 0.76 milliarcseconds. The entire interferometer telescope will allow 0.1 milliarcsecond resolution images of stellar surfaces and the universe in general to be taken.[32-34] It is estimated that PFP thrusters can provide pointing accuracy to within 2×10^{-9} degrees or 0.0072 milliarcseconds or 7.2 microarcseconds for a cubeSat. Each mirror sat will be a 1 m diameter mirror segment only a few times larger than a cubeSat so it is reasonable to expect a "mirror sat" employing PFP thrusters to have pointing accuracies comparable to those predicted for a cubeSat.

VI. Conclusion

The results for plasmonic space propulsion are very exciting. Plasmonic force propulsion can significantly enhance the state-of-the-art in small spacecraft position and attitude control by 1-2 orders of magnitude. PFP thrusters are a promising new propulsion system for both cubeSats and other small satellites which can be used as both an RCS and ACS. They require no power, and are extremely low mass and volume. Their low thrust and short switching time makes them ideal for missions where exact distances between spacecraft must be maintained or missions which require extremely high pointing capabilities. A cubeSat employing PFP thrusters would be able to maintain an attitude which was only limited by its attitude sensing instruments.

Results have elucidated the design geometry and configuration for a plasmonic force propulsion thruster, and led to a conceptual design. A single plasmonic force propulsion thruster should consist of many individual asymmetric nanostructures arranged in a multi-stage, layered, array. Nanostructures should be arranged end-to-end in series to form a multi-stage because a single nanostructure produces very small force and multiple stages are necessary to achieve useable thrust and exit velocity. Multi-stage nanostructures should be layered (i.e., stacked) on top of each other. Each layer should be designed to resonate at a different wavelength within the broadband solar spectrum. This will maximize use of the broadband solar spectrum as shorter wavelength light is absorbed/resonates with top layers, while longer wavelength light passes through to resonate with lower layers. Finally, the multi-stage layers of nanostructures should be repeated in an array to provide increased thrust.

Results for a conceptual design of a plasmonic thruster that has 35 layers, 86 array columns, multi-stage length of 5 mm, a 5-cm-diameter light focusing lens, and uses 100 nm polystyrene nanoparticles expelled at a rate of 1×10^{6} per sec would have a thrust of 250 nN, specific impulse of 10 sec, and minimum impulse bit of 50 pN-s. The thruster mass and volume are estimated at 100 g and 50 cm^3, respectively.

Plasmonic propulsion is ideally suited for proximity and attitude control maneuvers where the total spacecraft delta-V is relatively small (on the order of 1 m/s, compared with high delta-V orbit raising/maintenance maneuvers ~10-100 m/s). Because of its lower dry mass, plasmonic propulsion has a lower wet system mass for missions

---

[††] http://hires.gsfc.nasa.gov/si/

requiring delta-V of 3 m/s or less. This is ideal for proximity and attitude control where single maneuvers are mm/s, not main propulsion for orbit raising/maintenance.

As a result of our study, the TRL of plasmonic force propulsion has been raised from 1 to 2. A practical application for the technology has been invented: space propulsion. This application is speculative, and the analytical and numerical studies presented here required assumptions without proof or detailed analysis. However, these studies show that plasmonic force propulsion has the potential to provide a 1-2 order of magnitude benefit in the precision pointing and proximity control for small spacecraft.

VII.   Future Work

Future efforts should focus on (1) further analyzing the concept within a mission context, (2) experimentally demonstrating nanoparticle acceleration with asymmetric nanostructures excited by the Solar spectrum, and (3) creating a roadmap for future development of supporting technologies. The combination of these future activities would raise the TRL to early 3.

The concept should be further analyzed within a mission context. An example specific nano/picosat mission should be determined and analyzed through detailed orbital dynamics calculations. This should include the effects of passing through Earth shadow, if necessary. A possible example mission might be the Stellar Imager, where nanometer level proximity control and 0.1 milliarcsecond pointing control are required between multiple nanosatellites.

Nanoparticle acceleration should be demonstrated experimentally using asymmetric nanostructures excited by the Solar spectrum. Individual asymmetric nanostructures relevant to plasmonic propulsion should be fabricated and characterized. Specifically the transmission spectrum of the nanostructure within the Solar spectrum should be characterized and compared with our numerical predictions reported here. Additionally, nanoparticle manipulation (acceleration) should be characterized and used to determine plasmonic force, which can then be compared with numerical predictions reported here.

A roadmap should be created for future development of supporting technologies. Supporting technologies necessary for plasmonic propulsion have been investigated (Ref. [12]), but a roadmap for future development is necessary. Important supporting technologies include large-scale nanostructure manufacturing, solar light distribution system (fiber optic) development, switching technology development (shutter, microblinds with electric glass), nanoparticle propellant reservoir and feed system development (high-pressure gas, plasmonic manipulation).

Acknowledgments

References

[1]DePasquale, D., Bradford, J., "Nano/Microsatellite Market Assessment," SpaceWorks, Atlanta, GA, Feb. 2013.

[2]"Global Horizons: United States Air Force Global Science and Technology Vision," AF/ST TR 13-01, United States Air Force Chief Scientist, June 2013.

[3]NASA, "2011 NASA Strategic Plan," http://www.nasa.gov/news/budget/index.html, 2011.

[4]Micci, M. M., Ketsdever, A. D., "Micropropulsion for Small Spacecraft," Progress in Aeronautics and Astronautics, Vol. 187, P. Zarchan, ed., American Institute of Aeronautics and Astronautics, Inc., Reston, VA, 2000.

[5]Juan, M. L., Righini, M., Quidant, R., "Plasmon nano-optical tweezers," *Nature Photonics*, Vol. 5, No. 6, pp. 349-356, 2011.

[6]Schuller, J. A., Barnard, E. S., Cai, W., Jun, Y. C., White, J. S., Brongersma, M. L., "Plasmonics for extreme light concentration and manipulation," *Nature Materials*, Vol. 9, No. 3, pp. 193-204, 2010.

[7]Yang, X., Liu, Y., Oulton, R. F., Yin, X., Zhang, X., "Optical Forces in Hybrid Plasmonic Waveguides," *Nano Letters*, Vol. 11, No. 2, pp. 321-328, Feb. 9, 2011.

[8]Pyatenko, A., Takeuchi, H., Chiba, S., Ohyama, Y., "Dispersion of fine powder agglomerates under microgravity," *AIChE Journal*, Vol. 47, No. 12, pp. 2696-2704, Dec. 2001.

[9]Thomas A. Moore. *Six Ideas That Shaped Physics, Unit N: The Laws of Physics are Universal.* McGraw-Hill, Second edition, 2003.

[10]Thomas A. Moore. *Six Ideas That Shaped Physics, Unit C: Conservation Laws Constrain Interactions.* McGraw-Hill, Second edition, 2003.

[11]George P Sutton, and Oscar Biblarz. *Rocket Propulsion Elements*. John Wiley & Sons, Inc., Eighth edition, 2010.

[12]Friz, P. D., "Improving Plasma Actuator Performance at Low Pressure, and an Analysis of the Pointing Capabilities of CubeSats using Plasmonic Force Propulsion (PFP) Thrusters," Masters Thesis, Dept. of Aerospace Engineering, Missouri University of Science and Technology, Rolla, Missouri, 2014.

[13]Boris Lamontagne, and Py Christophe. Microblinds and a method of fabrication thereof. 2006.

[14]Alexey Shashurin, and Michael Keidar, and Taisen Zhuang. Comparative analysis of micro-cathode arc thruster performance. *33rd International electric Propulsion Conference*, Washington D.C., 2013. IEPC, Paper 2013-389.

[15]Taisen Zhuang, and Alexey Shashurin, and Isak Beilis, and Michael Keidar. Ion velocities in a micro-cathode arc thruster. *Physics of Plasmas*, 19(063501), 2012.

[16]Michael Keidar, and Samudra Haque, and Taisen Zhuang, and Alexey Shashurin, and Dereck Chiu, and George Teel. Micro-Cathode Arc Thruster for PhoneSat Propulsion. *27th Annual AIAA/USU Conference on Small Satellites*, Logan, Utah, 2013. Paper SSC13-VII-9.

[17]Taisen Zhuang, and Alexey Shashurin, and Samudra Haque and Michael Keidar. Performance characterization of the micro-Cathode Arc Thruster and propulsion system for space applications. *46th AIAA Joint Propulsion Conference and Exhibit*, Nashville, TN, 2010. AIAA 2010-7018.

[18]Alameda Applied Sciences Corporation. http://www.aasc.net/micropropulsion/vat/vat-specifications. Accessed: 2014-04-17.

[19]J. Schein, and N. Qi, and R. Binder, and M. Krishnan, and J. K. Ziemer, and J. E. Polk, and A. Anders. Inductive energy storage driven vacuum arc thruster. *Review of Scientific Instruments*, 73(2):925-927, 2002.

[20]Jochen Schein, and Niansheng Qi, and Robert Binder, and Mahadevan Krishahnan, and John Ziemer, and James Polk, and Andre Anders. Low Mass Vacuum Arc Thruster System for Station Keeping Missions. *IEPC-01-228*, Pasadena, CA, 2001. International Electric Propulsion Confrence.

[21]Tamer Akan, and Serdar Demirkol, and Naci Ekem, and Suat Pat, and Geavit Musa. Study of Metal and Ceramic Thermionic Vacuum arc Discharges. *Plasma Science and Technology*, 9(3):280-283.

[22]M. Coletti, and F. Guarducci, and S. B. Gabriel. A micro PPT for Cubesat application: Design and preliminary experimental results. *Elsevier*, 69:200-208, 2011.

[23]Clyde Space and Mars Space LTD. http://www.clyde-space.com/cubesat_shop/propulsion/303_cubesat-pulse-plasma-thruster. Accessed: 2013-11-18.

[24]Tom Roy, and Vlad Hruby, and Nathan Rosenblad, and Peter Rostler, and Douglas Spence. CubeSat Propulsion Using Electrospray Thrusters. *23rd Annual AIAA/USU Conference on Small Satellites*, 2009. SSC09-II-6.

[25]F. Martel, and P. Lozano. Ion Electrospray thruster Assemblies for CubeSats. *iCubeSat Workshop*, Cambridge, 2012. Massachusetts Institute of Technology.

[26]J. Mueller, and J. Ziemer, and R. Hofer, and R. Wirz, and T. O. Donnell. A Survey of Micro-Thrust Propulsion Options for Microspacecraft and Formation Flying Missions. *CubeSat 5th Annual Developers Workshop*, San Luis Obispo, CA, 2008. California Polytechnic State University.

[27]L. F. Velasquez-Garcia, and A. I. Akinwande, and M. Martinez-Sanchez. A Planar Array of Micro-Fabricated Electrospray Emitters for Thruster Applications. *Journal of Microelectromechanical Systems*, 15(5):1272-1280, 2006.

[28]Blue Canyon Technologies. www.bluecanyontech.com. Accessed: 2014-04-17.

[29]Meredith Gibb. LISA Laser Interferometer Space Antenna Project Office. http://lisa.nasa.gov/. Accessed: 2014-04-17.

[30]LISA: Study of the Laser Interferometer Space Antenna, Final Technical Report. *astrium*, 13631/99/NL/MS(LI-RP-DS-009), 2000.

[31]NASA, and esa. Laser Interferometer Space Antenna (LISA) Mission Concept. (LISA-PRJ-RP-0001), 2009.

[32]Kenneth Carpenter. SI: The Stellar Imager. http://hires.gsfc.nasa.gov/si/. Accessed: 2014-04-17.

[33]Kenneth G. Carpenter *et. al.* SI-The Stellar Imager: A UV/Optical deep-space telescope to image stars and oberve the Universe with 0.1 milli-arcsec angular resolution. 2005.

[34]Jorgen Christensen-Dalsgaard, and Kenneth G Carpenter, and Carlus J Schrijver, and Margarita Karovska, and the SI Team. The Stellar Imager (SI) - A Mission to Resolve Stellar Surfaces, Interiors, and Magnetic Activity. *Journal of Physics: Confrence Series*, 271(012085), 2011.